International Journal of Applied Earth Observation and Geoinformation 39 (2015) 79–87

Contents lists available at ScienceDirect

International Journal of Applied Earth Observation and Geoinformation

journal homepage: www.elsevier.com/locate/jag

Combining UAV-based plant height from crop surface models, visible, and near infrared vegetation indices for biomass monitoring in barley

Juliane Bendig[a,*], Kang Yu[a], Helge Aasen[a], Andreas Bolten[a], Simon Bennertz[a], Janis Broscheit[a], Martin L. Gnyp[a,b,c], Georg Bareth[a,c]

[a] Institute of Geography, GIS & RS Group, University of Cologne, Albertus-Magnus-Platz, 50923 Cologne, Germany
[b] Research Centre Hanninghof, Yara International ASA, Hanninghof 35, 48249 Dülmen, Germany
[c] ICASD-International Center for Agro-Informatics and Sustainable Development, College of Resources and Environmental Sciences, China Agricultural University, Beijing 100193, China

ARTICLE INFO

Article history:
Received 4 November 2014
Accepted 26 February 2015
Available online 10 March 2015

Keywords:
Point cloud
Structure from motion
Green red vegetation index
GnyLi
SAVI
NDVI

ABSTRACT

In this study we combined selected vegetation indices (VIs) and plant height information to estimate biomass in a summer barley experiment. The VIs were calculated from ground-based hyperspectral data and unmanned aerial vehicle (UAV)-based red green blue (RGB) imaging. In addition, the plant height information was obtained from UAV-based multi-temporal crop surface models (CSMs). The test site is a summer barley experiment comprising 18 cultivars and two nitrogen treatments located in Western Germany. We calculated five VIs from hyperspectral data. The normalised ratio index (NRI)-based index GnyLi (Gnyp et al., 2014) showed the highest correlation (R^2 = 0.83) with dry biomass. In addition, we calculated three visible band VIs: the green red vegetation index (GRVI), the modified GRVI (MGRVI) and the red green blue VI (RGBVI), where the MGRVI and the RGBVI are newly developed VI. We found that the visible band VIs have potential for biomass prediction prior to heading stage. A robust estimate for biomass was obtained from the plant height models (R^2 = 0.80–0.82). In a cross validation test, we compared plant height, selected VIs and their combination with plant height information. Combining VIs and plant height information by using multiple linear regression or multiple non-linear regression models performed better than the VIs alone. The visible band GRVI and the newly developed RGBVI are promising but need further investigation. However, the relationship between plant height and biomass produced the most robust results. In summary, the results indicate that plant height is competitive with VIs for biomass estimation in summer barley. Moreover, visible band VIs might be a useful addition to biomass estimation. The main limitation is that the visible band VIs work for early growing stages only.

1. Introduction

It is a well-known fact that biomass estimation is crucial for yield prediction of crops (Oerke et al., 2010). Crop parameters, like biomass, are frequently used to assess crop health status, nutrient supply and effects of agricultural management practices (Adamchuk et al., 2010). For management optimization, the nitrogen nutrition index (NNI) plays a key role (Chen et al., 2010; Tremblay et al., 2011). Biomass is needed for calculating the NNI (Lemaire and Gastal, 1997). A well-established method for biomass estimation is the calculation of vegetation indices (VIs) in the near infrared region (NIR) (Qi et al., 1994; Rouse et al., 1974), here defined as the range between 700 and 1300 nm (Kumar et al., 2001). Field spectroradiometers are commonly used for the collection of hyperspectral reflectance data that are used for such calculations (Clevers and Jongschaap, 2001; Kumar et al., 2001; Royo and Villegas, 2011).

An alternative possibility is to model biomass using plant height information. Lumme et al. (2008) and Tilly et al. (2014) demonstrated the suitability of the method in wheat, oat, barley and paddy rice. Plant height information is most useful when it is available at high spatial and temporal resolution. The method of multi-temporal crop surface models (CSMs) derived from 3D point clouds delivers the desired centimeter resolution (Bendig et al., 2013; Tilly et al., 2014). The method was studied for different crops by Hoffmeister et al. (2013, 2010),) for sugar beet, Tilly et al. (2014)

* Corresponding author. Tel.: +49 221 470 6551; fax: +49 221 470 4917.
E-mail addresses: juliane.bendig@uni-koeln.de (J. Bendig), kyu@uni-koeln.de, janis.b@arcor.de (K. Yu), helge.aasen@uni-koeln.de (H. Aasen), andreas.bolten@uni-koeln.de (A. Bolten), s.bennertz@gmail.com (S. Bennertz), martin.gnyp@yara.com (M.L. Gnyp), g.bareth@uni-koeln.de (G. Bareth).

http://dx.doi.org/10.1016/j.jag.2015.02.012
0303-2434/

for paddy rice and Bendig et al. (2014, 2013),) for summer barley. For small fields of a few hectares, suitable data collection platforms can be ground-based like terrestrial laser scanners (i.e., Hoffmeister et al., 2013; Tilly et al., 2014) or airborne like unmanned aerial vehicles (UAVs) (Bendig et al., 2014, 2013). Through the availability of high resolution consumer digital cameras, red green blue (RGB) aerial imaging with cm-resolution can easily be obtained using UAVs (D' Oleire-Oltmanns et al., 2012; Lucieer et al., 2014; Neitzel and Klonowski, 2012). At the same time, the emergence of structure from motion (SfM)-based software (Dandois and Ellis, 2010; Verhoeven, 2011) has enabled efficient creation of 3D point clouds and super high detail orthophotos.

Visible band VIs (VI_{RGB}) may be calculated from the orthophotos as demonstrated by Hunt et al. (2014, 2005). Motohka et al. (2010) used RGB-imagery obtained from a tower. These are some of the rare examples for small-scale field trials. Near infrared VIs (VI_{NIR}) are more widely used because of the characteristic difference between red and NIR reflection in green vegetation (Bannari et al., 1995). In addition, smaller, but significant spectral differences in the visible bands exist, which are caused by biochemical plant constituents such as chlorophyll (Hatfield et al., 2008; Roberts et al., 2011).

Collecting RGB-imagery by UAV is simple, cost-effective and VI_{RGB} can easily be calculated from the imagery. Consequently, the goal of this study is to investigate if UAV-based VI_{RGB} can compete with VI_{NIR} for biomass estimation. Crop monitoring by UAV-based RGB imagery enables obtaining the VI_{RGB} and the plant height information from the same dataset suggesting to combine both parameters to improve biomass estimation. According to Koppe et al. (2013), a combination of hyperspectral satellite imagery and radar can improve the model quality of biomass prediction. The objective of this study is to build up on this approach of combining the two parameters plant height and vegetation indices for biomass estimation by developing suitable regression models for UAV-based non-calibrated RGB imagery and ground-based hyperspectral reflectance data. We investigate the combination of VI_{NIR} and VI_{RGB} with CSM-based plant height information.

2. Materials and methods

2.1. Test Site

The study site is based at the Campus Klein-Altendorf agricultural research station (50°37′N, 6°59′E, altitude 186 m), located 40 km south of Cologne, Germany. In 2013, 18 summer barley (*Hordeum vulgare*) cultivars were planted, of which 10 were new cultivars and eight were old cultivars (Fig. 1, Bendig et al., 2014). They were treated with two levels of nitrogen fertilizer (40 and 80 kg N/ha). The experiment was organized in 36 small 3 × 7 m plots with a randomised order of the cultivars. Seedlings were planted with 300 plants/m^2 and a row spacing of 0.104 m. In addition, the plots are divided into a 3 × 5 m measuring area for plant height (PH) and reflectance measurements, and a 3 × 2 m sampling area for destructive biomass sampling. Biomass samples were taken frequently from April to July in 36 of the plots. For the UAV image collection, ground control points (GCPs) were evenly distributed across the field (Fig. 1). The positions were taken using a HiPer® Pro Topcon DGPS (Topcon Corporation, Tokyo, Japan) with 0.01 m horizontal and vertical precision. Later, the GCPs were identified in the images and used for georeferencing.

2.2. Biomass sampling and BBCH measurements

A destructive sample of 0.2 × 0.2 m above ground biomass was taken in the sampling area for each date (Fig. 1). The sampling dates were within one day before or after the UAV campaigns and the field spectroradiometer measurements. For the fresh biomass, the samples were cleaned, the roots were clipped and stem, leaves and ears were weighed. In a next step, the samples were dried at 70 °C for 120 h and dry biomass was weighed again for each plant. The weights were extrapolated to kg/m^2 for analysis. Plant growth stages were determined according to the 10 principal growth stages and 10 secondary growth stages of the "Biologische Bundesanstalt, Bundessortenamt und CHemische Industrie" (BBCH) scale

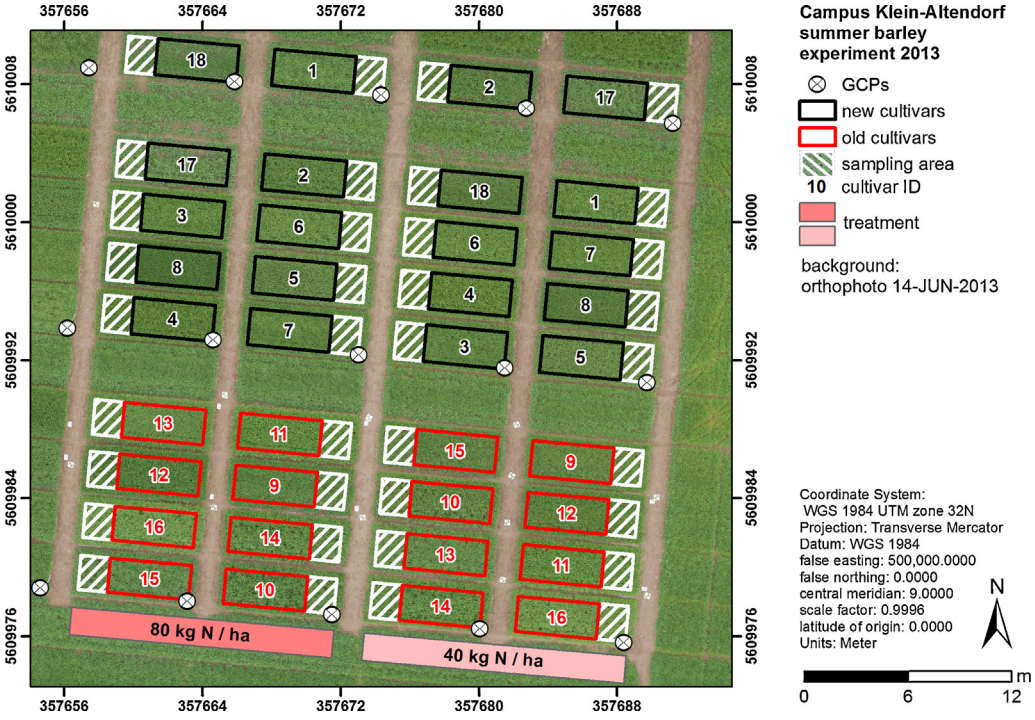

Fig. 1. Test site: summer barley experiment at Campus Klein-Altendorf agricultural research station in 2013 (Bendig et al., 2014); GCPs = ground control points used for crop surface model (CSM) generation.

Table 1
Near infrared vegetation indices (VI_{NIR}) used in this study where R = reflectance (%), R_R = red (630–690 nm), R_i = reflectance in a narrow band e.g. R_{1220} = 1220 nm, L = constant (modified from Huete, 1988)

VI	Name	Formula	References
NDVI	Normalized Difference Vegetation Index	$\frac{R_{900}-R_{680}}{R_{900}+R_{680}}$	(Peñuelas et al., 1993; Rouse et al., 1974)
SAVI	Soil Adjusted Vegetation Index	$(1+L)x\frac{R_{800}-R_{670}}{R_{800}-R_{670}+L}$	(Huete, 1988)
MSAVI	Modified SAVI	$0.5\left(2R_{800}+1-\sqrt{(2xR_{800}+1)^2-8(R_{800}-R_{670})}\right)$	(Qi et al., 1994)
OSAVI	Optimized Soil-Adjusted Vegetation Index	$(1+0.16)x\frac{R_{800}-R_{670}}{R_{800}+R_{670}+0.16}$	(Rondeaux et al., 1996)
GnyLi	Named by the developers Gnyp and Li	$\frac{R_{900}xR_{1050}-R_{955}xR_{1220}}{R_{900}xR_{1050}+R_{955}xR_{1220}}$	(Gnyp et al., 2014)

(Lancashire et al., 1991) along with PH measurements. Three plant representatives for the crop stand were chosen for each plot.

2.3. UAV-based data collection

The UAV used in this study was a multi-rotor MK-Oktokopter by HiSystems GmBH (Bendig et al., 2013). It is equipped with an RGB-sensor, a 16 Megapixel Panasonic Lumix GX1 (F1.7 aspheric (ASPH) fixed 20 mm lens) digital camera that is attached to the UAV on a gimbal. The gimbal compensates for the UAV movement (pitch and roll) during the flight and guarantees close to nadir image collection (Bendig et al., 2014). To trigger the sensor, we used the UAV's remote control. An autopilot was used for waypoint navigation to achieve the desired coverage of the AOI. On 30 April 2013, a bare ground ground model was recorded in a flight. Data from six flights (15, 28 May, 14, 25 June, 08 and 23 July) were used for the plant height derived from the CSM (PH_{CSM}).

Images were captured at 2 frames per second (fps) at 50 m above ground level (AGL). Camera settings were adjusted to lighting conditions and set to a fixed exposure for each flight, thus the settings changed between acquisition dates. The shutter speed varied from 1/400 s to 1/3200 s and the aperture was set to f/2.0 or f/2.8. Identical camera settings were used on three dates with shutter speed 1/1000 s and aperture f/2.0. The images were recorded during homogeneous and stable radiation conditions.

2.4. Field spectroradiometer measurements

Barley canopy reflectance was sensed with an ASD FieldSpec3 spectroradiometer (Analytical Spectral Devices, Inc., Boulder, CO, USA). The FieldSpec3 is a passive field device that is dependent on solar or artificial illumination. The spectroradiometer acquired the reflectance in the wavelength domain of 350–2500 nm with three detectors, one for the visible near infrared (VNIR: 350–1000 nm) and two for shortwave-infrared (SWIR1: 100–1830 nm, SWIR2: 1831–2500 nm). The FieldSpec3 has a 1.4 nm sampling interval in the VNIR and 2 nm sampling interval in the SWIR. Within the manufacturer's software the bands were resampled to a resolution of 1 nm. For continuous measurements of the same footprint, the spectroradiometer's fibre probe was fixed on an orthogonal frame with a 1 m sensor-canopy distance (Laudien and Bareth, 2006), and the same field of view of 25° was used. Hence, the acquisition geometry is described by sensor-canopy distance and field of view, resulting in a 0.155 m^2 sample area with a 44 cm diameter at the barley canopy surface.

Reflectance measurements were taken between 11 a.m. and 2 p.m. local mean time under solar illumination at the study site. Calibration measurements were carried out with a Spectralon (polytetrafluoroethylene (PTFE)) reference panel (white color) and a dark current at least every 10–15 min, depending on illumination changes. In the ASD RS3 software, twenty sample counts were set for a calibration and ten sample counts for the reflectance measurements at each scanning position of the barley canopy. Within one experimental plot, six scanning positions with representative plant growth were selected randomly and the six reflectance measurements were averaged to one value.

2.5. Plant height generation from CSM

In a first step, the collected images were mosaiced in the structure from motion (SfM)-based software Agisoft PhotoScan Professional (Verhoeven, 2011). For georeferencing the mosaic, the GCP positions were imported, manually placed on one image and automatically projected to the remaining images (Lucieer et al., 2014). Additionally, the positions were checked and adjusted manually. The software uses matching features in the images to perform a bundle adjustment and generates a point cloud (Sona et al., 2014). Finally, a digital surface model in *TIF image format is exported, which contains the crop surface model (CSM) information at a 0.01 m resolution. In addition, orthophotos are generated using the software's 'mosaicing blending mode'. In this mode, the software uses the pixel value of the most appropriate photo, in the case of overlapping photos, to calculate the orthophoto (Agisoft LLC, 2014). The orthophoto is then exported in *TIF image format at 0.01 m resolution for the VI_{RGB} calculations.

For the derivation of the PH_{CSM}, we used the workflow in Esri ArcGIS® 10.2.1 described in Bendig et al. (2013). An area of interest (AOI) is defined by the outline of the measuring area of the plots, which is buffered by a 0.3 m inside buffer to exclude the plot boundaries and the sampling area. To get information of the PH, each CSM (for each date) was subtracted from a bare ground model (Bendig et al., 2014). In a last step, the mean PH_{CSM} for each plot was averaged for each date.

2.6. Vegetation indices

2.6.1. Near infrared vegetation indices

In this study, we examined the correlation of different near infrared vegetation indices (VI_{NIR}), which are reported to be well correlated with biomass or leaf area index (LAI) (Thenkabail et al., 2000). These are the normalized difference vegetation index (NDVI), the soil adjusted vegetation index (SAVI), modified SAVI (MSAVI) and optimized SAVI (OSAVI) (Table 1). The NDVI (Rouse et al., 1974) is the most popular VI (Pettorelli, 2013), but its applicability is limited by atmospheric influences, soil reflectance in the spectra and saturation with the occurrence of high biomass values in later growth stages (Carlson and Ripley, 1997; Haboudane, 2004). The SAVI (Huete, 1988), MSAVI (Qi et al., 1994) and OSAVI (Rondeaux et al., 1996) are based on the NDVI but include correction factors for the soil reflectance in the spectra. In addition, we calculated the GnyLi (Gnyp et al., 2014) that is based on the normalised ratio index (NRI) equation (Thenkabail et al., 2000). The GnyLi exploits the difference of two reflectance and absorption features around 900 and 1200 nm. The reflectance peak at 900 nm is caused by the intercellular plant structure, while the reflection minimum between 970 and 1200 nm is affected by plant moisture, cellulose, starch and lignin (Curran, 1989; Pu et al., 2003).

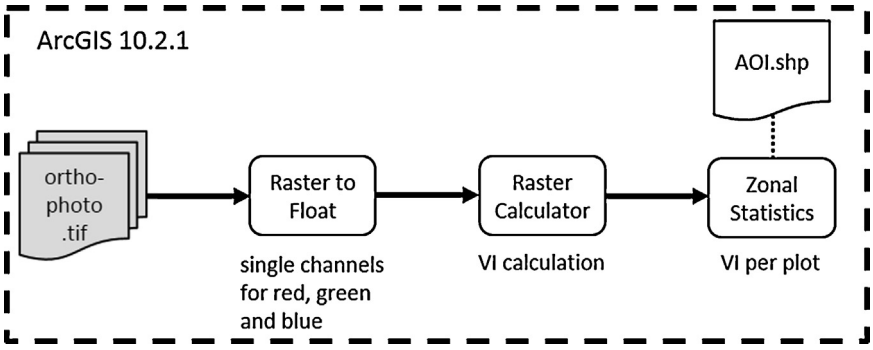

Fig. 2. Workflow for VI_{RGB} calculation. (AOI = old and new cultivars in Fig. 1).

In contrast to NDVI, SAVI, MSAVI and OSAVI, the GnyLi is calculated from narrow bands in the NIR domain only.

2.6.2. Visible band vegetation indices

Three VI_{RGB} were calculated from the orthophotos (Table 2) based on the NDVI equation (Motohka et al., 2010; Tucker, 1979). The green red vegetation index (GRVI) (Tucker, 1979) is used as a phenology indicator and has potential for biomass estimation (Hunt et al., 2005). It exploits the high reflectance of plants in the green (around 540 nm) and the absorption in the red and blue part of the visible spectrum (400–700 nm) through plant chlorophylls (Gao, 2006; Gitelson et al., 2002; Motohka et al., 2010). Squaring the band reflectance values helps to amplify the differences between red, green and blue reflectance. Based on these assumptions, we developed two new VIs. The modified GRVI (MGRVI) is defined as the normalized difference of the squared green reflectance and the squared red reflectance. To capture reflectance differences due to chlorophyll a-absorption (420, 490 and 660 nm) and chlorophyll b-absorption (435, 643 nm) (Kumar et al., 2001), we further introduced the new red green blue vegetation index (RGBVI). The RGBVI is defined as the normalized difference of the squared green reflectance and the product of blue × red reflectance (Table 2).

To calculate the VI_{RGB} we processed the above mentioned orthophotos in Esri ArcGIS® 10.2.1 by using the program's ModelBuilder. We extracted the digital numbers (DN) for each band (red, green and blue) by converting the *.TIF files to float files (*.FLT) (Fig. 2). The equations in Table 2 served as input to the raster calculator that was used to calculate the VI_{RGB}. To obtain the mean for each plot, we used the command 'zonal statistics as table'. We repeated the process for each VI_{RGB} and each orthophoto by employing an iterator.

2.7. Statistical analyses

The statistical analyses were executed in Microsoft® Excel® 2013 and IBM® SPSS® Statistics 22.0.0.0. Depending on the growth stages, we calculated a simple linear regression or exponential regression (Hansen and Schjoerring, 2003) for dry biomass and the VIs and PH_{CSM} (Table 3). To investigate the influence of combing VIs and PH_{CSM} we computed a multiple linear regression (MLR). Previous studies have shown that the relationships between the biomass and VIs or PH are often non-linear (Thenkabail et al., 2000). Therefore, a multiple non-linear regression (MNLR) model was employed to estimate the biomass. The non-linear model is a quadratic regression model (Berthold and Hand, 2006) using two variables and it takes the form of the following equation,

$$y = \beta_0 + \beta_1 x_{PH} + \beta_2 x_{VI} + \beta_3 x_{PH} x_{VI} + \beta_4 {x_{PH}}^2 + \beta_5 {x_{VI}}^2$$

where y is the biomass, and x_{PH} and x_{VI} are the PH_{CSM} and VI values, respectively. The model coefficients (β_0,...,β_5) were determined for the non-linear regression model based on the calibration dataset. All processes of the non-linear model were implemented in the SPSS software package.

Table 2
Visible band vegetation indices (VI_{RGB}) used in this study where R = reflectance (%), R_R = red, R_G = green, R_B = blue. Red Green and Blue are the DN values in the respective channels extracted from the orthophotos.

VI	Name	Formula	References
GRVI	Green Red Vegetation Index	$\frac{R_G - R_R}{R_G + R_R}$	(Tucker, 1979)
MGRVI	Modified Green Red Vegetation Index	$\frac{(R_G)^2 - (R_R)^2}{(R_G)^2 + (R_R)^2}$	Introduced here
RGBVI	Red Green Blue Vegetation Index	$\frac{(R_G)^2 - (R_B * R_R)}{(R_G)^2 + (R_B * R_R)}$	Introduced here

3. Results

3.1. Plant height and biomass samples

On each flight date between 200 and 800 photos of the field were taken, resulting in a point density between 2653 and 3452 (pts./m^2) and a mean of >9 images covering the same part of the AOI. To cover the AOI, we undertook two consecutive flights with an average 5 min flight time per flight on each date around 9 am local mean time (2 pm on 14 July). Lighting conditions were homogeneous for all flights except 25 June. On 25 June, the lighting conditions changed between flight one and flight two. We excluded images from the second flight to maintain radiation homogeneity. From 25 June onwards, lodging occurred in the plots with cultivars 10, 11, 12 and 14 (Fig. 1, details in (Bendig et al., 2014)), resulting in lower PH and reflection changes in the affected plots. The average measured PH_{CSM} varies between 0.14 and 1.00 m with a standard error (SE) of 0.25 m. The biomass samples of plots 7 and 46 on 08 July were identified as erroneous and therefore excluded from further analysis. The averaged dry biomass ranges from 0.03 to 2.70 kg/m^2 with a SE of 0.68 kg/m^2.

3.2. Biomass modelling

3.2.2. Model development

Biomass modelling was carried out from 15 May until 08 July 2013 ('all data'). On 23 July, the ripening crop substantially yellowed (BBCH Stages 77–89) and was thus unsuitable for biomass estimation from VIs. The results presented below are divided into 'all data' (n = 178) and 'pre heading' (n = 108), with 'pre heading' covering 15 May until 16 June 2013, due to significantly changing performance of the VI_{RGB} with the beginning of the heading stage. The general relationship between dry biomass and the VIs or the PH_{CSM} has an exponential trend in the 'all data' class and a linear trend in the 'pre heading' class.

Table 3
Coefficient of determination (R^2) and root mean square error (RMSE) for regression between dry biomass and either CSM derived plant height (PH_{CSM}) or near infrared (VI_{NIR}) or visible band (VI_{RGB}) vegetation indices where n = number of samples; ER = exponential regression and LR = linear regression.

VI/PH_{CSM} *versus* dry biomass		Exponential regression (ER)				Linear regression (LR)			
		All data		Pre heading		All data		Pre heading	
		n = 178		n = 108		n = 178		n = 108	
		R^2	RMSE (kg/m^2)	R^2	RMSE (kg/m^2)	R^2	RMSE (kg/m^2)	R^2	RMSE (kg/m^2)
PH_{CSM}		0.85	0.324	0.81	0.112	0.65	0.311	0.85	0.083
VI_{NIR}	GnyLi	0.83	0.35	0.76	0.119	0.62	0.326	0.71	0.113
	NDVI	0.4	0.515	0.61	0.162	0.16	0.484	0.39	0.164
	SAVI	0.59	0.468	0.7	0.144	0.3	0.441	0.51	0.147
	MSAVI	0.6	0.466	0.7	0.144	0.32	0.437	0.52	0.146
	OSAVI	0.54	0.481	0.68	0.148	0.25	0.457	0.47	0.153
VI_{RGB}	GRVI	0.13	0.596	0.79	0.117	0	0.528	0.62	0.13
	MGRVI	0.13	0.596	0.79	0.117	0	0.528	0.61	0.131
	RGBVI	0.41	0.439	0.67	0.156	0.33	0.434	0.47	0.153

Table 4
Cross-validation relationships between observed and predicted biomass (kg/m^2) for selected vegetation indices, PH_{CSM} respectively and combinations of both; ER = exponential regression; MLR = multiple linear regression, LR = linear regression; MNLR = multiple non-linear regression; n = number of samples; SE = standard error; R^2 = coefficient of determination; RMSE = root mean square error; RE = relative error.

Observed *versus* predicted biomass			Regression model	n	SE (kg/m^2)	R^2	RMSE (kg/m^2)	RE (%)
All data	ER	PH_{CSM}	BIOM = 0.070 × exp(PH_{CSM} × 4.155)	40	0.56	0.80	0.24	44.61
		GnyLi	BIOM = 0.025 × exp(GnyLi × 11.757)	40	0.52	0.65	0.30	56.45
		MSAVI	BIOM = 0.001 × exp(MSAVI × 6.436)	40	0.40	0.22	0.46	86.84
		GRVI	BIOM = 0.187 × exp(GRVI × 5.594)	40	0.39	0.00	0.53	99.87
		RGBVI	BIOM = 0.062 × exp(RGBVI × 3.553)	40	0.47	0.59	0.32	61.18
	MNLR	GnyLi + PH_{CSM}	BIOM = 0.073 + (1.206 × PH_{CSM}) + (-2.678 × GnyLi) + (-11.109 × (PH_{CSM} × GnyLi)) + (2.743 × PH_{CSM}^2) + (21.811 × GnyLi^2)	40	0.59	0.74	0.26	48.86
		MSAVI + PH_{CSM}	BIOM = 1.321 + (4.243 × PH_{CSM}) + (-3.910 × MSAVI) + (-4.403 × (PH_{CSM} × MSAVI)) + (2.050 × PH_{CSM}^2) + (2.865 × MSAVI^2)	40	0.60	0.77	0.25	47.87
		GRVI + PH_{CSM}	BIOM = 0.052 + (3.146 × PH_{CSM}) + (-2.229 × GRVI) + (-3.172 × (PH_{CSM} × GRVI)) + (-1.200 × PH_{CSM}^2) + (1.439 × GRVI^2)	40	0.58	0.74	0.26	49.10
		RGBVI + PH_{CSM}	BIOM = 0.404 + (1.664 × PH_{CSM}) + (-2.332 × RGBVI) + (0.275 × (PH_{CSM} × RGBVI)) + (-0.285 × PH_{CSM}^2) + (2.508 × RGBVI^2)	40	0.61	0.84	0.21	40.69
Pre heading	LR	PH_{CSM}	BIOM = 1.009 × PH + 0.018	24	0.22	0.81	0.09	45.01
		GnyLi	BIOM = 2.651 × GnyLi-0.196	24	0.24	0.74	0.10	51.30
		MSAVI	BIOM = 1.074 × MSAVI-0.651	24	0.23	0.72	0.11	55.34
		GRVI	BIOM = 2.240 × GRVI-0.032	24	0.24	0.76	0.10	54.22
		RGBVI	BIOM = 0.878 × RGBVI-0.140	24	0.23	0.64	0.10	53.21
	MLR	GnyLi + PH_{CSM}	BIOM = 0.909 × PH_{CSM} + 0.324 × GnyLi-0.014	24	0.22	0.82	0.09	44.43
		MSAVI + PH_{CSM}	BIOM = 1.139 × PH_{CSM}-0.220 × MSAVI + 0.174	24	0.22	0.78	0.09	44.24
		GRVI + PH_{CSM}	BIOM = 1.077 × PH_{CSM}-0.206 × GRVI + 0.029	24	0.22	0.79	0.09	45.01
		RGBVI + PH_{CSM}	BIOM = 1.111 × PH_{CSM}-0.158 × RGBVI + 0.067	24	0.22	0.78	0.09	45.79

The coefficients of determination (R^2) for the exponential regression (ER) and linear regression (LR) between the PH_{CSM} and dry biomass and VIs and dry biomass are presented in Table 3. We classified R^2 in high (>0.7), medium (0.5 < R^2 < 0.7) and low (<0.5) correlation. In the ER 'all data' class, high correlations were found between PH_{CSM} (R^2 = 0.85) and the GnyLi (R^2 = 0.83). All other combinations yielded medium correlations (SAVI, MSAVI and OSAVI, R^2 = 0.54-0.6) or low correlations (NDVI, GRVI, MGRVI, RGBVI, R^2 = 0.12-0.41). In the LR of 'pre heading' growth stages we found a high correlation between dry biomass and PH_{CSM} (R^2 = 0.85) and GnyLi (R^2 = 0.71). All other relationships were medium (SAVI, MSAVI, GRVI, MGRVI, R^2 = 0.51–0.62) or low (NDVI, RGBVI, R^2 = 0.39–0.47).

3.2.2. Model application

Based on the results from Table 3, PH_{CSM}, GnyLi, MSAVI, GRVI and RGBVI were selected for model application. The dataset was divided into a calibration and validation dataset. The validation dataset consisted of the randomly selected cultivars 1, 6, 13 and 18 (two old and two new cultivars), while the remaining cultivars served for the calibration. We developed exponential regression and multiple non-linear regression (MNLR) models for the 'all data' class and linear regression and multiple linear regression (MLR) models for the 'pre heading' class. The calibration models (Table 4) were then applied to the validation datasets and evaluated by the relation between observed and predicted biomass (Figs. 3 and 4,).

In the 'all data' class (Fig. 3), the PH_{CSM} model had a high fit with R^2 = 0.80 and a low relative error (RE) of 44.61%. Comparably high fits were found for the MNLR model combinations of GnyLi + PH_{CSM} (R^2 = 0.74, RE = 48.86%) and MSAVI + PH_{CSM} (R^2 = 0.77, RE = 47.86%) and RGBVI + PH_{CSM} (R^2 = 0.84, RE = 40.69%). The R^2 in the 'pre heading' dataset (Fig. 4) were all above 0.64 with RE under 55.34%. The highest fit occurred for the GnyLi + PH_{CSM} MLR model (R^2 = 0.82, RE = 44.43%).

4. Discussion

The primary aim of this study is to evaluate UAV-based RGB imaging and two of its products: the plant height (PH) and VI_{RGB}. Both are available at cm-resolution derived from imagery acquired

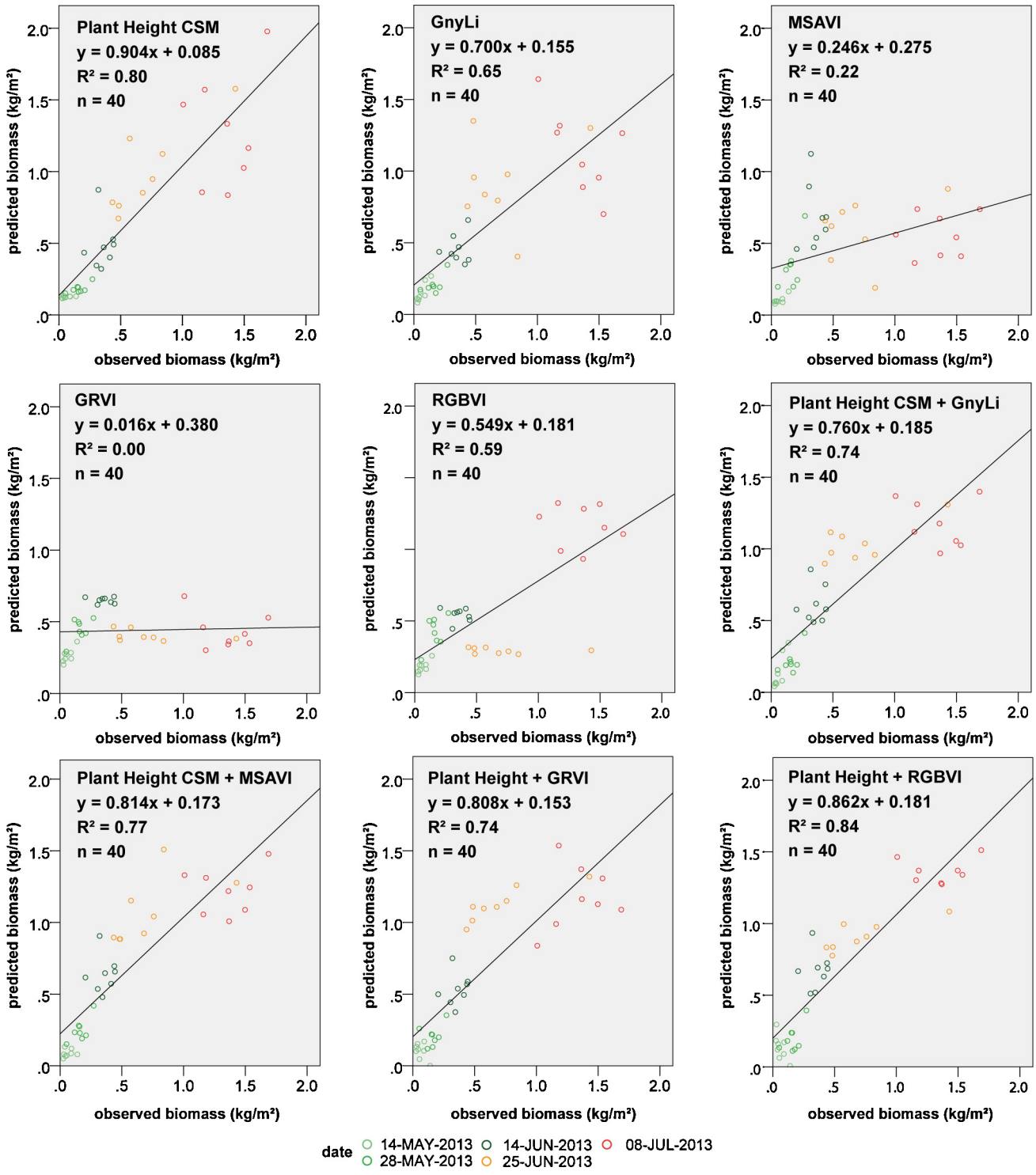

Fig. 3. 'All data' class cross-validation scatter plots for observed dry biomass *versus* predicted biomass derived from validation datasets listed in Table 4; $p < 0.0001$ for all R^2.

by a low flying multi-rotor UAV. We compared the performance in biomass estimation of PH, VI_{RGB}, high spectral resolution VI_{NIR} from point measurements, and the combination of the VIs with PH. It appears from the results in Tables 3 and 4 that CSM-derived plant height (PH_{CSM}) and GnyLi are the most robust parameters for biomass estimation in summer barley, while PH_{CSM} performs slightly better than GnyLi. In addition, combinations of PH_{CSM} with VI_{RGB} or VI_{NIR} performed better than the VIs alone. In early growth stages, only the combination of GnyLi + PH_{CSM} ($R^2 = 0.82$) yielded a slightly higher R^2 than the PH_{CSM} ($R^2 = 0.81$). Although, the RGBVI + PH_{CSM} produces a higher R^2 than the PH_{CSM} across all growth stages, this result should be regarded with caution. The performances of the VI_{RGB} vary significantly between model development and model application due to a small calibration and validation set. Thus, strong relationships in model applications might be produced randomly. Generally, the statistically more complex MLR and MNLR produce robust results, but a more significant improvement was expected. Positive examples for combining remotely sensed information from different sources are found in the literature (Koppe et al., 2013; Liu et al., 2006). Most

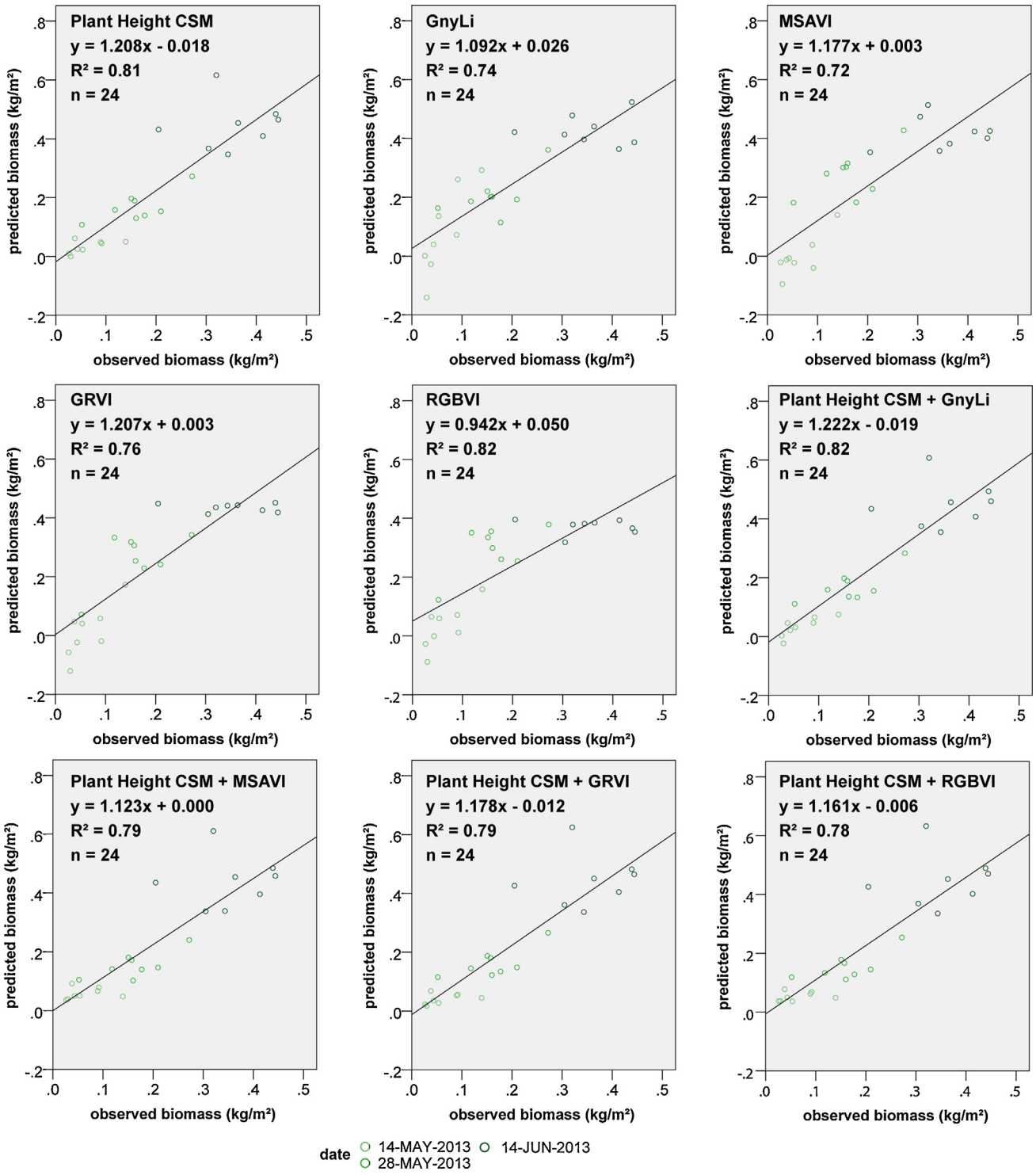

Fig. 4. 'Pre heading' class cross-validation scatter plots for observed dry biomass *versus* predicted biomass derived from validation datasets listed in Table 4; $p < 0.0001$ for all R^2.

studies comparable to this one either investigate the relationship between PH and biomass (i.e. Ehlert et al., 2008; Lumme et al., 2008) or the relationship between VIs and biomass (i.e., Hunt et al., 2005; Motohka et al., 2010; Tucker, 1979). Geipel et al. (2014) investigated yield prediction from UAV-based CSMs and VI_{RGB} for early growth stages in maize. They found a slightly higher correlation (up to $R^2 = 0.74$) between yield and PH_{CSM} in combination with one of three tested VI_{RGB}.

Of the VI_{NIR} investigated here, the GnyLi clearly outperformed the NDVI-based indices. This result is consistent with a multi-scale study for winter wheat, where the GnyLi outperformed 14 other indices (Gnyp et al., 2014). The NDVI-based indices perform lower, due to the well-known saturation effect. Similar results are reported by (Baret and Guyot, 1991; Gnyp et al., 2014; Haboudane, 2004; Mutanga and Skidmore, 2004). According to the statistics, the GRVI and MGRVI showed no correlation and the RGBVI

produced a low correlation to the biomass after the booting stage (14 June 2013). Nevertheless, high positive correlations were found until booting stage, which is important for fertilizer management to improve crop yield. Management recommendations show that summer barley is commonly fertilized after seeding and at the tillering stage (Munzert and Frahm, 2006). Additionally, Chang et al. (2005) state that the booting stage is best suited for yield prediction using canopy reflectance. Similarly, studies in different crops and grasses by Motohka et al. (2010), Hunt et al. (2005) and Tucker (1979) demonstrate that the applicability of VI_{RGB} is limited to certain growth stages.

Generally, there are noteworthy constraints in the VI_{RGB} generation method. We collected images with fixed exposure under homogeneous radiation conditions. We then calculated the VI_{RGB} from an image mosaic. Minor changes in radiation can cause varying RGBVI values. As a result, there is no radiometric correction for changes in lighting conditions between single photos. Changing light incidence introduces bidirectional reflectance distribution function (BRDF) effects, even in close to nadir imaging (Grenzdörffer and Niemeyer, 2011). Capturing the whole AOI in one image can partly eliminate the problem. Furthermore, no calibration between the images was possible because no object of known reflectance was present, like e.g. calibration panels or colored tarpaulins. Moreover, no investigation was made of the exact wavelengths covered by the red, green and blue bands of the digital camera. On the one hand, a calibration of digital numbers (DN) in the images with a monochromatic light source is highly recommended (Hunt. et al., 2005). On the other hand, a comparison of RGBVI values calculated from the field spectroradiometer and the UAV-based data yielded an R^2 of 0.9 for the early growth stages. Ultimately, multi-year studies are required to evaluate and improve the method for obtaining VI_{RGB} from UAV-based RGB imagery.

Practically speaking, the data collection for hyperspectral reflectance data with a field spectroradiometer is more complex and time-consuming than the data collection with a UAV-system. A field spectroradiometer produces point data, while UAV-based imaging has the advantage of capturing infield variability faster and with a dense spatial coverage. Moreover, a field spectroradiometer is a sensitive and expensive instrument that requires significant expertise. A spectroradiometer's main advantage is the high spectral resolution of calibrated spectra. On the other hand an out-of-the-box UAV-system can be operated by a larger user group at a low cost. Moreover, with an 800€ sensor plant height can be measured and biomass can be estimated almost as good as with VI_{NIR} from the spectroradiometer.

5. Conclusions and outlook

In this study, we examined the suitability of plant height and vegetation indices in the visible and near infrared region in their suitability for biomass prediction in a summer barley experiment. The statistical analysis showed that the GnyLi near infrared index is a suitable indicator for biomass as well as unmanned aerial vehicle-derived plant height from crop surface models. Secondly, there is potential for biomass estimation by combining plant height and visible band vegetation indices like Green Red Vegetation Index (GRVI), newly developed Modified Green Red Vegetation Index (MGRVI), and Red Green Blue Vegetation Index (RGBVI). We found that the visible band indices showed a better ability to model biomass in early growth stages in comparison to late growth stages. Contrary to expectation, the combination of vegetation indices and plant height did not significantly improve the model performance.

Using an unmanned aerial vehicle with a non-calibrated optical camera to calculate visible band vegetation indices and plant height is a unique way to estimate biomass on small agricultural research fields. It is a simple and timely alternative to cost-intensive and complex ground-based reflectance measurements.

Future studies should examine these simple and cost effective method for multiple year datasets to improve robustness and applicability. In addition, new hyperspectral full frame cameras for unmanned aerial vehicles are a promising development for research in near infrared vegetation indices by combining high spectral and spatial resolution, opening up new possibilities in crop monitoring.

Acknowledgments

The authors acknowledge the funding of the CROP.SENSe.net project in the context of the Ziel 2-Programm North Rhine-Westphalia (NRW) 2007–2013 "Regionale Wettbewerbsfähigkeit und Beschäftigung (Europäischer Fonds für regionale Entwicklung (EFRE))" by the Ministry for Innovation, Science and Research (Ministerium für Innovation, Wissenschaft und Forschung (MIWF)) of the state North Rhine-Westphalia (NRW) and European Union Funds for regional development (EFRE)(005-1103-0018).

References

Adamchuk, V.I., Ferguson, R.B., Hergert, G.W., 2010. Soil heterogeneity and crop growth. In: Oerke, E.-C., Gerhards, R., Menz, G., Sikora, R.A. (Eds.), Precision Crop Protection – The Challenge and Use of Heterogeneity. Springer, Dordrecht, Netherlands, pp. 3–16.

Agisoft LLC, 2014. Agisoft PhotoScan [WWW Document]. Agisoft PhotoScan. URL http://www.agisoft.com (accessed 10.9.14.).

Bannari, A., Morin, D., Bonn, F., Huete, A.R., 1995. A review of vegetation indices. Remote Sens. Rev. 13, 95–120, http://dx.doi.org/10.1080/02757259509532298.

Baret, F., Guyot, G., 1991. Potentials and limits of vegetation indices for LAI and APAR assessment. Remote Sens. Environ. 35, 161–173, http://dx.doi.org/10.1016/0034-4257(91)90009-U.

Bendig, J., Bolten, A., Bareth, G., 2013. UAV-based imaging for multi-temporal, very high resolution crop surface models to monitor crop growth variability. Photogramm. – Fernerk. – Geoinf. 6, 551–562, http://dx.doi.org/10.1127/1432-8364/2013/0200.

Bendig, J., Bolten, A., Bennertz, S., Broscheit, J., Eichfuss, S., Bareth, G., 2014. Estimating biomass of barley using crop surface models (CSMs) derived from UAV-based rgb imaging. Remote Sens. 6, 10395–10412, http://dx.doi.org/10.3390/rs61110395.

Berthold, M.R., Hand, D., 2006. Intelligent Data Analysis, 2nd ed. Springer, Berlin, Germany.

Carlson, T.N., Ripley, D.A., 1997. On the relation between NDVI, fractional vegetation cover, and leaf area index. Remote Sens. Environ. 62, 241–252, http://dx.doi.org/10.1016/S0034-4257(97)00104-1.

Chang, K.-W., Shen, Y., Lo, J.-C., 2005. Predicting rice yield using canopy reflectance measured at booting stage. Agron. J. 97, 872, http://dx.doi.org/10.2134/agronj2004.0162.

Chen, P., Haboudane, D., Tremblay, N., Wang, J., Vigneault, P., Li, B., 2010. New spectral indicator assessing the efficiency of crop nitrogen treatment in corn and wheat. Remote Sens. Environ. 114, 1987–1997, http://dx.doi.org/10.1016/j.rse.2010.04.006.

Clevers, J.P.G.W., Jongschaap, R., 2001. Imaging spectrometry for agricultural applications. In: Meer, F.D., van der, Jong, S.M.D. (Eds.), Imaging Spectrometry, Remote Sensing and Digital Image Processing. Kluwer Academic Publishers, Dordrecht, Netherlands, pp. 157–199.

Curran, P.J., 1989. Remote sensing of foliar chemistry. Remote Sens. Environ. 30, 271–278, http://dx.doi.org/10.1016/0034-4257(89)90069-2.

Dandois, J.P., Ellis, E.C., 2010. Remote sensing of vegetation structure using computer vision. Remote Sens. 2, 1157–1176, http://dx.doi.org/10.3390/rs2041157.

D' Oleire-Oltmanns, S., Marzolff, I., Peter, K., Ries, J., 2012. Unmanned aerial vehicle (UAV) for monitoring soil erosion in Morocco. Remote Sens. 4, 3390–3416, http://dx.doi.org/10.3390/rs4113390.

Ehlert, D., Horn, H.-J., Adamek, R., 2008. Measuring crop biomass density by laser triangulation. Comput. Electron. Agric. 61, 117–125, http://dx.doi.org/10.1016/j.compag.2007.09.013.

Gao, J., 2006. Canopy Chlorophyll Estimation with Hyperspectral Remote Sensing (Dissertation). Kansas State University, Manhattan, Kansas, US.

Geipel, J., Link, J., Claupein, W., 2014. Combined spectral and spatial modeling of corn yield based on aerial images and crop surface models acquired with an unmanned aircraft system. Remote Sens. 6, 10335–10355, http://dx.doi.org/10.3390/rs61110335.

Gitelson, A.A., Kaufman, Y.J., Stark, R., Rundquist, D., 2002. Novel algorithms for remote estimation of vegetation fraction. Remote Sens. Environ. 80, 76–87, http://dx.doi.org/10.1016/s0034-4257(01)289-9.

Gnyp, M.L., Bareth, G., Li, F., Lenz-Wiedemann, V.I.S., Koppe, W., Miao, Y., Hennig, S.D., Jia, L., Laudien, R., Chen, X., Zhang, F., 2014. Development and implementation of a multiscale biomass model using hyperspectral vegetation indices for winter wheat in the North China Plain. Int. J. Appl. Earth Observ. Geoinform. 33, 232–242, http://dx.doi.org/10.1016/j.jag.2014.05.006.

Grenzdörffer, G.J., Niemeyer, F., 2011. UAV based BRDF-measurements of agricultural surfaces with PFIFFIKUS. International archives of the photogrammetry. Remote Sens. Spatial Inform. Sci. XXXVIII-1/C22, 229–234.

Haboudane, D., 2004. Hyperspectral vegetation indices and novel algorithms for predicting green LAI of crop canopies: modeling and validation in the context of precision agriculture. Remote Sens. Environ. 90, 337–352, http://dx.doi.org/10.1016/j.rse.2003.12.013.

Hansen, P.M., Schjoerring, J.K., 2003. Reflectance measurement of canopy biomass and nitrogen status in wheat crops using normalized difference vegetation indices and partial least squares regression. Remote Sens. Environ. 86, 542–553, http://dx.doi.org/10.1016/S0034-4257(03)131-7.

Hatfield, J.L., Gitelson, A.A., Schepers, J.S., Walthall, C.L., 2008. Application of spectral remote sensing for agronomic decisions. Agron. J. 100, S117–S131, http://dx.doi.org/10.2134/agronj2006.0370c.

Hoffmeister, D., Bolten, A., Curdt, C., Waldhoff, G., Bareth, G., 2010. High-resolution Crop Surface Models (CSM) and Crop Volume Models (CVM) on field level by terrestrial laser scanning. In: Guo, H., Wang, C. (Eds.), SPIE Proceedings of the Sixth International Symposium on Digital Earth: Models, Algorithms, and Virtual Reality. Presented at the Sixth International Symposium on Digital Earth: Models, Algorithms, and Virtual Reality, Beijing, China, pp. 78400E–78400E6, http://dx.doi.org/10.1117/12.872315.

Hoffmeister, D., Waldhoff, G., Curdt, C., Tilly, N., Bendig, J., Bareth, G., 2013. Spatial variability detection of crop height in a single field by terrestrial laser scanning. In: Stafford, J.V. (Ed.), Precision Agriculture '13. Presented at the 9th European Conference on Precision Agriculture. Wageningen Academic Publishers, Lleida, Spain, pp. 267–274.

Huete, A.R., 1988. A soil-adjusted vegetation index (SAVI). Remote Sens. Environ. 25, 295–309, http://dx.doi.org/10.1016/0034-4257(88) 90,106-X.

Hunt, E., Daughtry, C., Mirsky, S., Hively, W., 2014. Remote sensing with simulated unmanned aircraft imagery for precision agriculture applications. IEEE J. Sel. Top. Appl. Earth Observ. Remote Sens., http://dx.doi.org/10.1109/JSTARS2014.2317876.

Hunt Jr., E.R., Cavigelli, M., Daughtry, C.S.T., McMurtrey III, J.E., Walthall, C.L., 2005. Evaluation of digital photography from model aircraft for remote sensing of crop biomass and nitrogen status. Precis. Agric. 6, 359–378, http://dx.doi.org/10.1007/s11119-005-2324-5.

Koppe, W., Gnyp, M.L., Hütt, C., Yao, Y., Miao, Y., Chen, X., Bareth, G., 2013. Rice monitoring with multi-temporal and dual-polarimetric TerraSAR-X data. Int. J. Appl. Earth Observ. Geoinform. 21, 568–576, http://dx.doi.org/10.1016/j.jag.2012.07.016.

Kumar, L., Schmidt, K., Dury, S., Skidmore, A., 2001. Imaging spectrometry and vegetation science. In: Meer, F.D., van der Jong, S.M.D. (Eds.), Imaging Spectrometry, Remote Sensing and Digital Image Processing. Kluwer Academic Publishers, Dordrecht, Netherlands, pp. 111–155.

Lancashire, P.D., Bleiholder, H., Boom, T.V.D., Langelüddeke, P., Stauss, R., Weber, E., Witzenberger, A., 1991. A uniform decimal code for growth stages of crops and weeds. Ann. Appl. Biol. 119, 561–601, http://dx.doi.org/10.1111/j.1744-7348.1991.tb04895.x.

Laudien, R., Bareth, G., 2006. Multitemporal hyperspectral data analysis for regional detection of plant diseases by using a tractor- and an airborne-based spectrometer. Photogramm. – Fernerk. – Geoinform. 3, 217–227.

Lemaire, G., Gastal, F., 1997. N uptake and distribution in plant canopies. In: Lemaire, D.G. (Ed.), Diagnosis of the Nitrogen Status in Crops. Springer, Berlin, Germany.

Liu, L., Wang, J., Bao, Y., Huang, W., Ma, Z., Zhao, C., 2006. Predicting winter wheat condition, grain yield and protein content using multi-temporal EnviSat-ASAR and Landsat TM satellite images. Int. J. Remote Sens. 27, 737–753, http://dx.doi.org/10.1080/01431160500296867.

Lucieer, A., Turner, D., King, D.H., Robinson, S.A., 2014. Using an Unmanned Aerial Vehicle (UAV) to capture micro-topography of Antarctic moss beds. Int. J. Appl. Earth Observ. Geoinform. 27, 53–62, http://dx.doi.org/10.1016/j.jag.2013.05.011.

Lumme, J., Karjalainen, M., Kaartinen, H., Kukko, A., Hyyppä, J., Hyyppä, H., Jaakkola, A., Kleemola, J., 2008. Terrestrial laser scanning of agricultural crops. The International Archives of the Photogrammetry. Remote Sens. Spatial Inform. Sci. 37, 563–566.

Motohka, T., Nasahara, K.N., Oguma, H., Tsuchida, S., 2010. Applicability of green–red vegetation index for remote sensing of vegetation phenology. Remote Sens. 2, 2369–2387, http://dx.doi.org/10.3390/rs2102369.

Munzert, M., Frahm, J., 2006. Pflanzliche Erzeugung: Grundlagen des Acker- und Pflanzenbaus und der Guten fachlichen Praxis, Grundlagen der Verfahrenstechnik, Produktions- und Verfahrenstechnik für Kulturpflanzen, Dauergrünland, Sonderkulturen, Nachwachsende Rohstoffe, Ökologischer Landbau, Naturschutz und Landschaftspflege, 12th ed. BLV, Munich, Germany.

Mutanga, O., Skidmore, A.K., 2004. Narrow band vegetation indices overcome the saturation problem in biomass estimation. Int. J. Remote Sens. 25, 3999–4014, http://dx.doi.org/10.1080/01431160310001654923.

Neitzel, F., Klonowski, J., 2012. Use of point cloud with a low-cost UAV system for 3D mapping, in: International Archives of the Photogrammetry, Remote Sensing and Spatial Information Science. Presented at the 2011 ISPRS Zurich 2011 Workshop, 14-16 September 2011, Zurich, Switzerland, Zurich, pp. 39–44.

Oerke, E.-C., Gerhards, R., Menz, G., Sikora, R.A. (Eds.), 2010. Springer, Dordrecht, Netherlands.

Peñuelas, J., Gamon, J.A., Griffin, K.L., Field, C.B., 1993. Assessing community type, plant biomass, pigment composition, and photosynthetic efficiency of aquatic vegetation from spectral reflectance. Remote Sens. Environ. 46, 110–118, http://dx.doi.org/10.1016/0034-4257(93)90,088-F.

Pettorelli, N., 2013. The Normalized Difference Vegetation Index. Oxford University Press, Oxford, UK.

Pu, R., Ge, S., Kelly, N.M., Gong, P., 2003. Spectral absorption features as indicators of water status in coast live oak (Quercus agrifolia) leaves. Int. J. Remote Sens. 24, 179–1810, http://dx.doi.org/10.1080/01431160210155965.

Qi, J., Chehbouni, A., Huete, A.R., Kerr, Y.H., Sorooshian, S., 1994. A modified soil adjusted vegetation index. Remote Sens. Environ. 48, 119–126, http://dx.doi.org/10.1016/0034-4257(94)90,134-1.

Roberts, D., Roth, K., Perroy, R., 2011. Hyperspectral vegetation indices. In: Thenkabail, P.S., Huete, A. (Eds.), Hyperspectral Remote Sensing of Vegetation. CRC Press, Boca Raton, FL, US, pp. 309–328.

Rondeaux, G., Steven, M., Baret, F., 1996. Optimization of soil-adjusted vegetation indices. Remote Sens. Environ. 55, 95–107, http://dx.doi.org/10.1016/0034-4257 (95) 186-7.

Rouse, J.W., Haas, R.H., Schell, J.A., Deering, D.W., 1974. Monitoring vegetation systems in the great plains with erts. NASA Special Publication 351, 309.

Royo, C., Villegas, D., 2011. Field measurements of canopy spectra for biomass assessment of small-grain cereals. In: Matovic, M.D. (Ed.), Biomass – Detection, Production and Usage. InTech, Rijeka, Croatia, pp. 27–52.

Sona, G., Pinto, L., Pagliari, D., Passoni, D., Gini, R., 2014. Experimental analysis of different software packages for orientation and digital surface modelling from UAV images. Earth Sci. Inform. 7, 97–107, http://dx.doi.org/10.1007/s12145-013-0142-2.

Thenkabail, P.S., Smith, R.B., De Pauw, E., 2000. Hyperspectral vegetation indices and their relationships with agricultural crop characteristics. Remote Sens. Environ. 71, 158–182, http://dx.doi.org/10.1016/S0034-4257 (99) 67-X.

Tilly, N., Hoffmeister, D., Cao, Q., Huang, S., Lenz-Wiedemann, V.I.S., Miao, Y., Bareth, G., 2014. 2014: Multitemporal crop surface models: accurate plant height measurement and biomass estimation with terrestrial laser scanning in paddy rice. J. Appl. Remote Sens. 8, 083671, http://dx.doi.org/10.1117/1. JRS.8.083671.

Tremblay, N., Fallon, E., Ziadi, N., 2011. Sensing of crop nitrogen status: opportunities, tools, limitations, and supporting information requirements. HortTechnology 21, 274–281.

Tucker, C.J., 1979. Red and photographic infrared linear combinations for monitoring vegetation. Remote Sens. Environ. 8, 127–150, http://dx.doi.org/10.1016/0034-4257(79) 90,013-0.

Verhoeven, G., 2011. Taking computer vision aloft – archaeological three-dimensional reconstructions from aerial photographs with photoscan. Archaeol. Prospect. 18, 67–73, http://dx.doi.org/10.1002/arp.399.